

# Geophysical Research Letters

## RESEARCH LETTER

10.1029/2020GL090014

### Key Points:

- Aerosol increases accumulative precipitation by a factor of 2T and invigorates lightning activities in Houston during Hurricane Harvey
- Observations show intense lightning over Houston which exhibits geographic similarity to climatological maximum lightning flash density
- To better forecast extreme weather events, it is essential to account for aerosol effects in operational weather forecast models

### Supporting Information:

- Supporting Information S1

### Correspondence to:

Y. Wang and R. Zhang,  
yuan.wang@caltech.edu;  
renyi-zhang@geos.tamu.edu

### Citation:

Pan, B., Wang, Y., Logan, T., Hsieh, J.-S., Jiang, J. H., Li, Y., & Zhang, R. (2020). Determinant role of aerosols from industrial sources in Hurricane Harvey's catastrophe. *Geophysical Research Letters*, 47, e2020GL090014. <https://doi.org/10.1029/2020GL090014>

Received 23 JUL 2020

Accepted 15 NOV 2020

Accepted article online 20 NOV 2020

### Author Contributions:

**Conceptualization:** Yuan Wang, Renyi Zhang

**Formal analysis:** Bowen Pan, Yuan Wang, Timothy Logan

**Methodology:** Bowen Pan, Yuan Wang

**Validation:** Bowen Pan, Yuan Wang, Jen-Shan Hsieh, Jonathan H. Jiang, Renyi Zhang

**Writing – original draft:** Bowen Pan, Yuan Wang, Renyi Zhang

## Determinant Role of Aerosols From Industrial Sources in Hurricane Harvey's Catastrophe

Bowen Pan<sup>1,2</sup> , Yuan Wang<sup>3,4</sup> , Timothy Logan<sup>1</sup> , Jen-Shan Hsieh<sup>1</sup>, Jonathan H. Jiang<sup>4</sup> , Yixin Li<sup>5</sup>, and Renyi Zhang<sup>1,5</sup> 

<sup>1</sup>Department of Atmospheric Sciences, Texas A&M University, College Station, TX, USA, <sup>2</sup>Department of Atmospheric Science, Colorado State University, Fort Collins, CO, USA, <sup>3</sup>Division of Geological and Planetary Sciences, California Institute of Technology, Pasadena, CA, USA, <sup>4</sup>Jet Propulsion Laboratory, California Institute of Technology, Pasadena, CA, USA, <sup>5</sup>Department of Chemistry, Texas A&M University, College Station, TX, USA

**Abstract** The destructive power of tropical cyclones is driven by latent heat released from water condensation and is inevitably linked to the abundance of aerosols as cloud condensation nuclei. However, the aerosol effects are unaccounted for in most operational hurricane forecast models. We combined multisource measurements and cloud-resolving model simulations to show fundamentally altered cloud microphysical and thermodynamic processes by anthropogenic aerosols during Hurricane Harvey. Our observational analyses reveal intense lightning and precipitation in the proximity of Houston industrial areas, and these hot spots exhibit a striking geographic similarity to a climatological maximum of lightning flash density in the south-central United States. Our ensemble cloud-resolving simulations of Hurricane Harvey indicate that aerosols increase precipitation and lightning by a factor of 2 in the Houston urban area, unraveling the key anthropogenic factor in regulating flooding during this weather extreme.

**Plain Language Summary** The catastrophic flooding during Hurricane Harvey has received major attention, but the cause remains mysterious. The destructive power of tropical cyclones is produced by the latent heat release from phase change of water, which is linked to airborne particles emitted from vehicles and petrochemical plants. By combining observation and model simulations, our work provides microphysical and thermodynamic insights into the cause of the catastrophic flooding during Hurricane Harvey by the aerosols from industrial sources. Our discovery underscores the importance of representing the effects of anthropogenic aerosols for accurate short-term forecast and climate projection of tropical cyclones to minimize future catastrophic destruction along the highly industrialized Gulf of Mexico region.

## 1. Introduction

Hurricane Harvey wreaked havoc on southeast Texas with heavy rainfall of about 555 mm in the Houston urban area (29.5–30.0°N, 95.9–95.2°W) during 25–28 August 2017. As large and complex low-pressure systems associated with high surface enthalpy flux (Figure 1a), the development, intensity, and precipitation of tropical cyclones were regulated by several meteorological and environmental parameters, including sea surface temperature (SST), vertical wind shear, vorticity, and humidity of the free troposphere (Emanuel, 2017). Several studies have linked Hurricane Harvey's devastation to climate change (Emanuel, 2017; van Oldenborgh et al., 2017) or changes in land use due to urbanization (Zhang et al., 2018). In particular, human-caused climate changes have been implicated for increasing intensity and destruction of tropical cyclones in recent decades, by inducing favorable conditions (increasing SST) to supercharge hurricanes and increasing the risk of major damage (Emanuel, 2005, 2017; Goldenberg et al., 2001; Patricola & Wehner, 2018; Trenberth, 2005; van Oldenborgh et al., 2017). However, whether the characteristics of tropical cyclones have changed or will change under a warming climate remains controversial (Knutson et al., 2010). In addition, urbanization causes changes in land use, which were attributed to exacerbating the rainfall and flooding of Hurricane Harvey along the highly urbanized coastal Houston area (Zhang et al., 2018). Another key feature of tropical cyclones is reflected by efficient formation of hydrometeors and enormously large release of latent heat to fuel the destruction, that is, storm surge, strong winds, and flooding. The amount of precipitation poured in the Houston urban area alone during this extreme event corresponds to an energy of about  $5.5 \times 10^{18}$  J estimated from water condensation. Currently, the relative

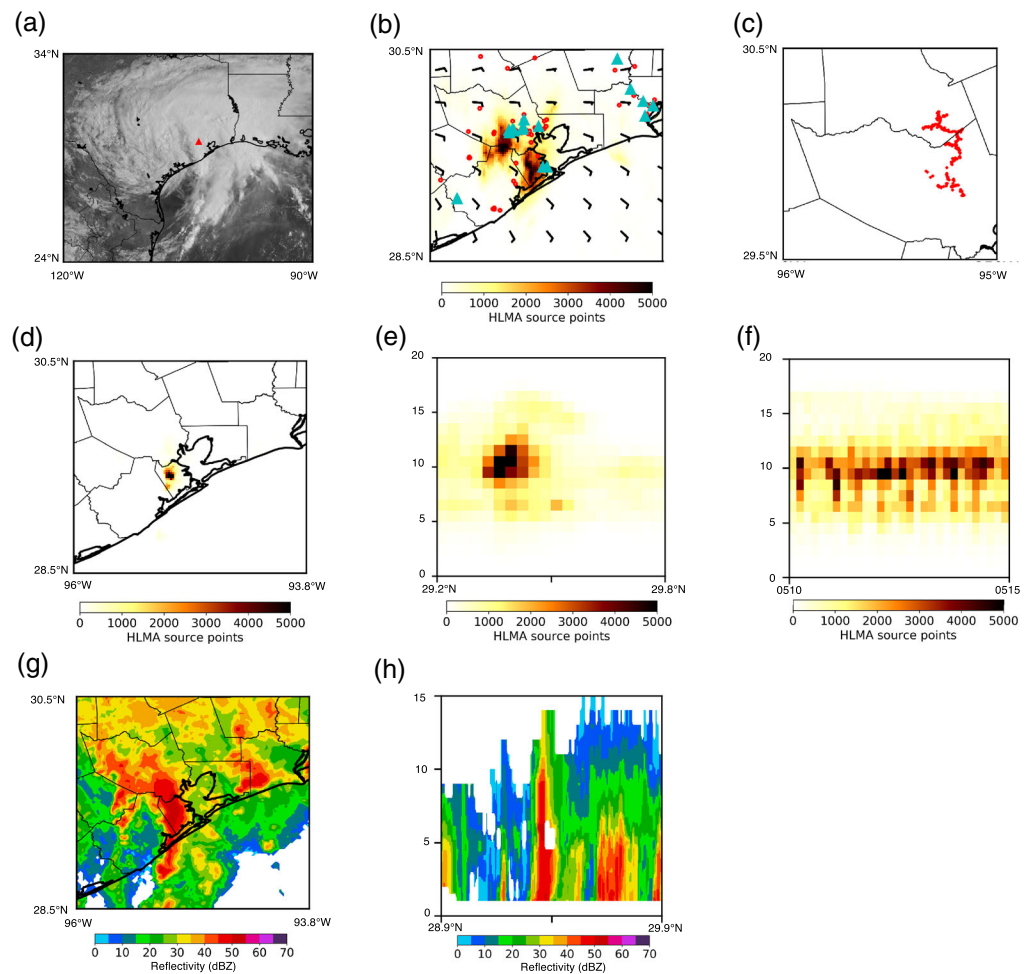


**Figure 1.** Intense lightning and precipitation in the Houston industrial proximity. (a) GOES-16 visible satellite image at 1504 UTC 27 August. The red triangle labels the location for the city of Houston. (b) Lightning distribution from HLMA on 27 August, which is overlaid with petroleum refineries (cyan triangles), power plants (red circles), and wind direction (black barbs). (c) A large lightning flash at 0300 UTC 27 August detected by HLMA. (d–h) An active storm episode at 0510–0515 UTC 27 August: horizontal distribution of HLMA source points (d), vertical zonal cross-section of HLMA source points (e), vertical time series of HLMA source points (f), base radar reflectivity in dBZ (g), and vertical cross-section of radar reflectivity in dBZ (h).

contributions of the various factors to regulating the destructive power of tropical cyclones remain to be quantified.

From a microphysical perspective, the phase transformation of water molecules from vapor to liquid or ice is nonspontaneous and hindered by profound thermodynamic (free energy) and kinetic (curvature effect) barriers (Zhang et al., 2012), and the presence of aerosols is needed to act as cloud condensation nuclei (CCN) for cloud formation, precipitation, and storm development (Fan et al., 2018; Wang et al., 2011). There has been accumulating evidence that natural and anthropogenic aerosols play critical roles in cloud-related phenomena (Fan et al., 2018; Wang et al., 2011) as well as the genesis (Pan et al., 2018) and development (e.g., Herbener et al., 2014; Khain et al., 2008; Lynn et al., 2016; Rosenfeld et al., 2012; Wang et al., 2014; Zhao et al., 2018) of tropical cyclones. However, most operational forecast (such as the Weather Research and Forecasting or WRF) models simulate the track and intensity of hurricanes using a prescribed number concentration of cloud droplets or a single moment microphysical scheme to represent the formation and growth of hydrometeors, which are insensitive to the aerosol effects (Zhang et al., 2018). Also, the number concentrations of CCN/cloud droplets in those models are typically fixed at a level characteristic of pristine maritime environments (Zhang et al., 2018) but significantly underrepresented over land, particularly in urban and industrial areas (Zhang et al., 2015).

As the country's fourth largest city, Houston hosts many industrial facilities, that is, power plants, chemical manufactories, and petroleum refineries (Fan et al., 2005) (Figures 1b and S1a). For example, the southeast Texas region (27–32°N and 94–98°W) is home to one of the world's most densely distributed (over 400) refineries, which comprise approximately 40% of the nation's petrochemical capacity with a daily production of 0.3 million barrels. As evident from satellite measurements and emission estimations (Figure S2), the mass concentration of fine particulate matter (smaller than 2.5  $\mu\text{m}$  or  $\text{PM}_{2.5}$ ) in Houston often exceeds the annual average level of the National Ambient Air Quality Standards (Fan et al., 2005; Levy et al., 2013). Ground-based measurements and model simulations showed that elevated levels of aerosols emitted from industry considerably influence convection, lightning, and precipitation in this region (Fan et al., 2007; Hu et al., 2020; Li et al., 2008, 2009; Orville et al., 2001). A recent study by Souri et al. (2020) simulated a moderate increase in precipitation by aerosols over Houston, but the model baseline simulation was not fully evaluated by observational data. In this study, we combine ground-based rain gauge and radar measurements, high-density lightning detection network, and satellite storm and lightning observations to characterize Hurricane Harvey. Cloud-resolving model simulations of Hurricane Harvey are systematically compared with available measurements. The model sensitivity experiments with different aerosol emission scenarios shed light on the impacts of anthropogenic aerosols on Hurricane Harvey.

## 2. Materials and Methods

### 2.1. Observational Data

The observed rainfall data were taken from the hourly Stage IV Precipitation NCEP/EMC 4KM Gridded Data. The Stage IV precipitation analysis was based on a combination of surface rain gauge measurements and radar calculated rainfall produced by 12 River Forecast Centers (RFCs) in the Contiguous United States. Each RFC manually quality controls the Multisensor Precipitation Estimates (MPE) precipitation data in its respective region before being included in the national Stage IV mosaic. The hourly analyses were used in this work.

The lightning source points and lightning events data were from the Houston Lightning Mapping Array (HLMA), National Lightning Detection Network (NLDN), and Geostationary Lightning Mapper (GLM) on the Geostationary Operational Environmental Satellite (GOES-16). The HLMA is a three-dimensional total lightning location system that includes 12 lightning detection stations within 200 km of Houston, providing total lightning mapping for the Houston region and southeast Texas. Each station includes a Very High Frequency (VHF; 60 MHz) time-of-arrival total lightning mapping sensors built by New Mexico Institute of Mining and Technology (Cullen, 2013). The sensor detects the time of arrival of a VHF impulse emitted as part of the electrical breakdown and lightning propagation process. Data from each sensor are processed on a central LMA server to provide three-dimensional mapping of these impulses, that is, LMA sources. The GLM, on board of the GOES-16, is a single-channel, near-infrared optical transient detector that can detect the momentary changes in an optical scene, indicating the presence of lightning. GLM measures the frequency, location, and extent of lightning discharges, as well as total lightning activities (in-cloud, cloud to cloud, and cloud to ground) with a near-uniform spatial resolution of approximately 10 km (GOES-R Algorithm Working Group and GOES-R Series Program, 2018). The NLDN consists of over 100 remote, ground-based sensing stations located across the United States that instantaneously detect the electromagnetic signals when lightning strikes occur (Orville et al., 2001). The spatial and temporal distributions of the LMA sources, NLDN strikes, and GLM level 2 lightning events were used in our analysis. The vertical cross-section and maximum radar reflectivity data were from the three-dimensional gridded Next Generation Weather Radar (NEXRAD; Bowman & Homeyer, 2017), that is, the Weather Surveillance Radar, 1988, Doppler (WSR-88D) network.

### 2.2. Model Configuration and Experiment Design

The cloud-resolving Weather Research and Forecasting model Version 3.6 (CR-WRF) was used for Hurricane Harvey simulations. The WRF model simulation was initialized at 0600 UTC 23 August 2017, and assimilated brightness temperature from the GOES-16 was used from 0600 UTC 23 August to 0000 UTC 25 August. The free-run simulation covered the period from 0000 UTC 25 August to 0000 UTC 28 August with two two-way nested vortex-following domains and horizontal grid spacings of 27, 9, and 3 km (Figure S2a). The sea surface temperature for the free-run was initiated from the Optimum

Interpolated daily sea surface temperature (Reynolds et al., 2007). For control and each sensitivity experiment, five ensemble simulations were performed, where the initial temperature field was randomly perturbed.

An aerosol-aware two-moment microphysics scheme was used in the CR-WRF simulations. A detailed description of this microphysical WRF framework has been described elsewhere (Li et al., 2008; Wang et al., 2014). Briefly, the mass-mixing ratio and number concentration of aerosols were predicted. Aerosols activated as CCN according to the Köhler theory once the supersaturation criteria were reached (Li et al., 2008). The microphysical scheme calculated the mass-mixing ratios and number concentrations of five different types of hydrometeors, including cloud droplet, raindrop, ice crystal, snow, and graupel. Ice nucleation processes included deposition/condensation, immersion, contact, and homogeneous freezing. Supersaturation and droplet diffusional growth are explicitly calculated in the scheme.

Two scenarios, a clean (C case) and a polluted case (P case), were considered to realistically represent the concentration, emission, and distribution of natural and anthropogenic aerosols over the model domain. Aerosols in both cases consisted of anthropogenic aerosols and sea-spray aerosols (SSA). The initial concentrations of anthropogenic aerosols in the Houston urban area were 209 and  $4,192\text{ cm}^{-3}$  for the C and P cases, respectively, according to field measurements in the Houston urban area (Levy et al., 2013). These initial concentrations of anthropogenic aerosols in the Houston urban area, along with the aerosol optical depth (AOD) measured by the Moderate Resolution Imaging Spectroradiometer (MODIS) from 17 to 24 August, were used to derive the geographic distribution of anthropogenic aerosols inside the outer domain ( $8^{\circ}\text{S}$  to  $52^{\circ}\text{N}$ ,  $13^{\circ}\text{--}118^{\circ}\text{W}$ ). Specifically, the initial concentrations of anthropogenic aerosols for the C and P cases at a grid point over land were calculated by multiplying the aerosol concentrations in the Houston urban area for the two cases to the ratio of the values of the local to Houston AOD over the outer domain. The initial concentrations of anthropogenic aerosols over ocean were determined according to the same procedure, except that smaller aerosol concentrations (by 10 times) were applied to the Houston values to reflect the land and ocean contrast. The SSA was uniformly distributed over land and ocean with the initial concentrations of 6 and  $60\text{ cm}^{-3}$ , respectively. A sea salt production scheme was included, where SSA was produced according to the wind speed (Wang et al., 2014). In addition, a constant emission rate of  $46\text{ kg s}^{-1}$  was implemented to the bottom 1 km of the atmosphere in the Houston urban area to account for continuous emission of anthropogenic aerosols during Hurricane Harvey. Such an aerosol emission rate was close to half of that ( $105\text{ kg s}^{-1}$ ) from the National Emission Inventory (U.S. Environmental Protection Agency, 2011) in the Houston urban area (Figure S2b). The SSA consisted of mainly sea salt with a hygroscopic parameter ( $\kappa$ ) value of 0.9, and the anthropogenic aerosols had a  $\kappa$  value of 0.53, characteristic of the aerosol hygroscopicity measured in the Houston region (Levy et al., 2013). The removal of aerosols included activation to form cloud droplets, but precipitation scavenging was not considered in the present simulations. Advection of aerosols from the lateral boundaries into the model domain occurred under favorable wind conditions. The vertical distribution of SSA and anthropogenic aerosols followed an exponential decay, with the highest concentration at the surface.

### 3. Results

To assess the impacts of anthropogenic aerosols to precipitation and lightning during Hurricane Harvey, we analyzed ground- and satellite-based lightning (Figures 1b–1f, S1b, and S1c) and ground-based radar reflectivity (Figures 1g and 1h) measurements. Highly intense lightning and radar reflectivity are evident in the southeast Texas region during 26–27 August. Measurements by the three-dimensional Houston Lightning Mapping Array (HLMA; Figure 1b), satellite Geostationary Lightning Mapper (GLM; Figure S1b), and National Lightning Detection Network (NLDN; Figure S1c) exhibit a similar spatiotemporal pattern of unusually active lightning at the location surrounded by the Houston industrial facilities. A total of 0.23 million (both intracloud and cloud-ground) lightning flashes were detected by the NLDN from 26 to 28 August, and over 12 million lightning source points were recorded by HLMA during 26–27 August. Also, the lightning flashes exhibited large horizontal and vertical extensions. For example, an individual lightning strike with a horizontal dimension exceeding 40 km occurred on 27 August (Figure 1c). From 0510 to 0515 UTC 27 August, the most active lightning occurred at  $29.4^{\circ}\text{N}$  and  $95.1^{\circ}\text{W}$  (Figure 1d) and extended vertically from 5 to 15 km, with the maximum intensity at 10 km (Figures 1e and 1f). The lightning hot spot (Figure 1d)



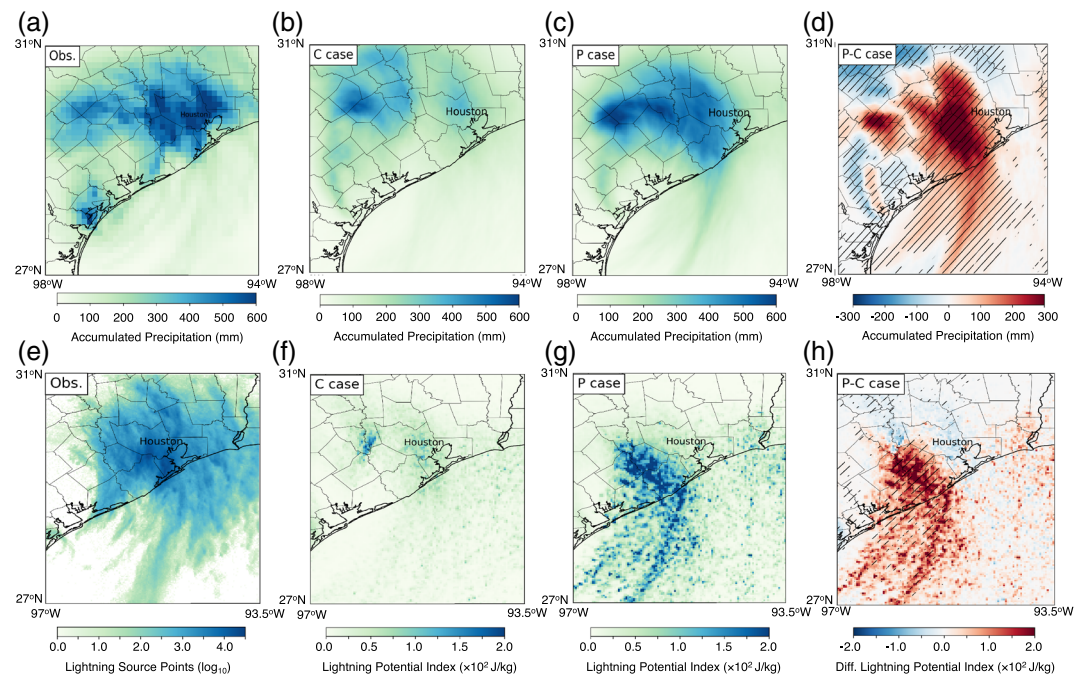


**Figure 2.** Aerosol-enhanced precipitation and lightning. (a–d) Observed and simulated accumulative precipitation (mm) from 0000 UTC 26 August to 0000 UTC 28 August: observation from the NCEP Stage IV data (a), C case (b), P case (c), and the difference between P and C cases (d). (e) GOES-16 GLM lightning events from 0000 UTC 26 August to 0000 UTC 28 August. (f–h) Simulated LPI from 0000 UTC 26 August to 2330 UTC 27 August: C case (f), P case (g), and the difference between the P and C cases (h). Hatched lines denote the significant difference between the P and C cases according to the Student's *t* test at the 95% confidence level.

collocated with the maximum radar reflectivity (Figure 1g). The vertical cross-section of radar reflectivity (Figure 1h) showed the maximum value of 50 dBZ reaching up to 10 km height, indicating the strongest precipitation and convective activity. Evidently, the geographic distributions of the lightning hotspot detected by the GLM, HLMA, and NLDN and the accumulative precipitation maximum (Figures 1b and S1b–S1d) during this event exhibit a striking similarity to a decadal climatological maximum lightning flash density in the south-central United States (Figure S1e; Orville et al., 2001).

Using a cloud-resolving WRF (CR-WRF) model, we quantified the aerosol effects on precipitation (Figures 2a–2d) and lightning (Figures 2e–2h) during Hurricane Harvey (Figure S3). Sensitivity simulations were performed under a clean (C) case to represent the pristine initial condition and a polluted (P) case to represent an elevated initial aerosol condition along with a continuous emission from the industrial sources (Figure S4). Specifically, our model simulations of the aerosol distributions, emissions, and properties were constrained by ground and satellite measurements in this region (Levy et al., 2013). Comparison between the C and P cases shows similar spatial distributions but distinct differences in the magnitude of precipitation. The accumulative precipitation during 26 and 28 August is much higher in the P case than in the C case (Figures 2b and 2c), and the difference between the two cases ranges from 100 to 350 mm in the Houston urban area (Figure 2d). The distribution and magnitude of precipitation in the P case are consistent with those from the observation (Figure 2a), while precipitation is significantly underpredicted in the C case.

Based on the modeled hydrometeor contents, we calculated a lightning potential index (LPI) to reflect charge separation and cloud electrification (Wang et al., 2011; details are provide in the supporting information). The LPI is highly elevated in the P case but is minimal in the C case (Figures 2f and 2g), with the largest difference by a factor of 3 (Figure 2h). The spatial distribution of enhanced LPI in the P case is also comparable to that of the lightning observation (Figure 2e).

The temporal evolution of the accumulative precipitation in the Houston urban area is comparable between the observation and P case, with the values of  $558 \pm 47$  and 600 mm, respectively, at 0000 UTC on 28 August (Figure 3a). In contrast, the accumulative precipitation ( $249 \pm 19$  mm) in the C case is less than half of those

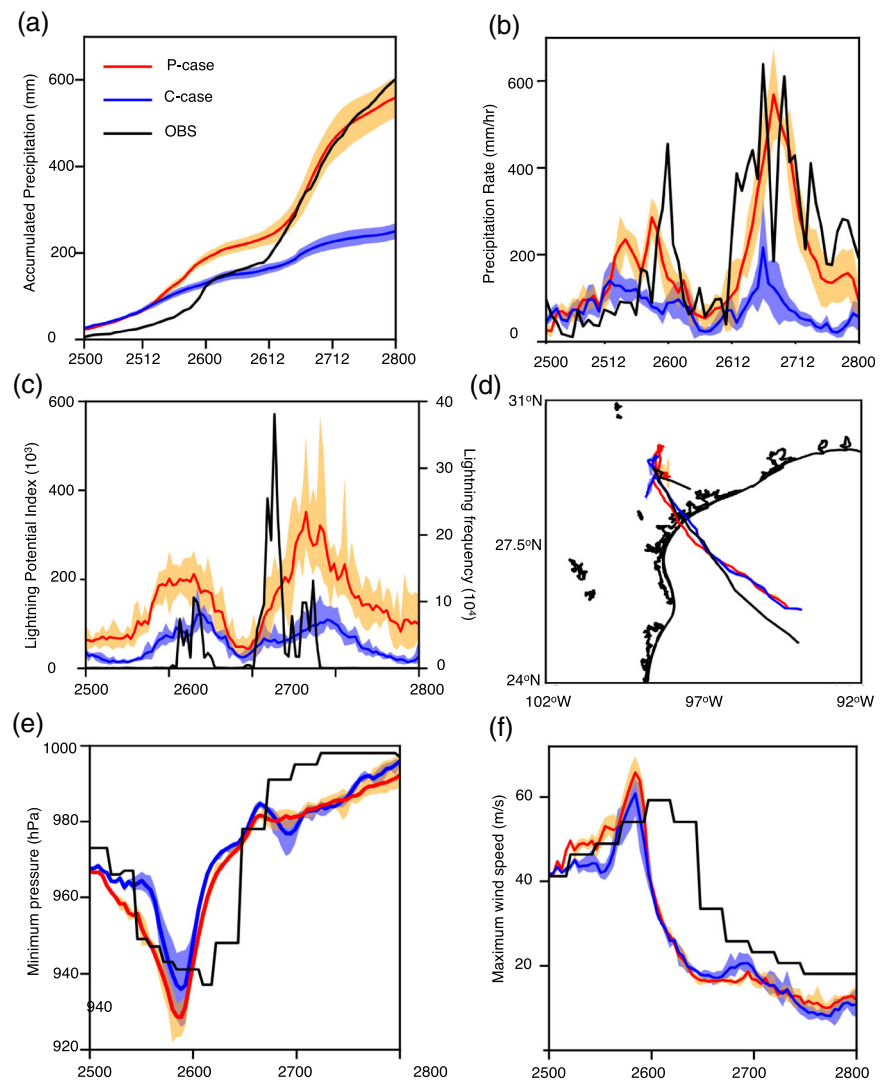


**Figure 3.** Aerosol effects on hurricane evolution. (a and b) Temporal evolution of the accumulative precipitation (a, mm) and precipitation rate (b,  $\text{mm hr}^{-1}$ ) in the Houston urban area, showing two intense precipitation periods, that is, during 1000–1300 UTC 26 August (Rain I) and 0000–1800 UTC 27 August (Rain II). The black curve corresponds to the measurements, and the blue and red curves denote the simulations in the C and P cases, respectively. (c) Temporal evolutions in simulated LPI (right y-axis) in C (blue) and P (red) cases and observed lightning frequency (left y-axis) by HLMA from 0000 UTC 26 August to 2330 UTC 27 August and in the southeast Texas region. (d) Comparison of the storm tracks between the observation and simulation in the C (blue) and P (red) cases. (e and f) Comparison of the minimum pressure (e, mb) and maximum wind speed (f,  $\text{m s}^{-1}$ ) between the observation and simulation in the C (blue) and P (red) cases. The x axis is labeled as DDHH, i.e., 2,500 for 0000 UTC 25 August. The results from a to b are averaged over the Houston urban area (Figure S3b). The shaded area in a–f denotes the range of deviation from the ensemble simulations.

of the observation and P case. The observed and simulated precipitation rates exhibit two intense periods (Figure 3b). The maximum precipitation rate ( $28 \pm 5 \text{ mm hr}^{-1}$ ) in the P case agrees with the observation ( $32 \text{ mm hr}^{-1}$ ), and both values are over a factor of 2 higher than that ( $11 \pm 6 \text{ mm hr}^{-1}$ ) in the C case. The temporal evolutions of the simulated LPI in the P and C cases are similar to the observation, while the LPI value is 2.8 times higher in the P case than in the C case (Figure 3c). The domain mean accumulated precipitation increase is about 29% (from  $\sim 138$  to  $\sim 178 \text{ mm}$ ).

We analyzed the microphysical and thermodynamic characteristics relevant to hydrometeors and latent heating profiles in the simulations. The vertical cross-sections of mixing ratios of liquid and ice hydrometeors in the P case are highly elevated between 2–4 and 6–12 km, respectively, and large latent heat is

released between 4 and 8 km (Figures S5a, S5b, S5d, and S5e). The largest difference in the latent heating rates between the P and C cases is up to  $10 \text{ K day}^{-1}$  (Figures S5c and S5f), corresponding to an increase of 250% in the P case. The averaged vertical distributions of ice hydrometeor mixing ratios and latent heating rates in the Houston urban area show higher values of both quantities in the P case than in the C case during the two intense precipitation periods (Figures S6a, S6b, S6g, and S6h). The maximum latent heating rate in the P case is about twofold higher than that in the C case, because of more condensation in the warm regime. The average water ( $S_w$ ) and ice ( $S_i$ ) supersaturation at  $-13^\circ\text{C}$  (or 7 km) over the Houston urban area are 0.16 and 0.03, respectively, in the P case (Figure S7), indicating condensational/depositional growth of supercooled water/ice hydrometeors and continuous latent heat release in the mixed-phase regime. The higher  $S_w$  and  $S_i$  values below/at the freezing level in the P case are attributed to a larger latent heat to yield stronger buoyancy (Figures S6a–S6d), which is augmented by strong cyclonic lifting (Figures 1a and 1b) and abundant moisture supply (Figure S1d). The  $S_w$  and  $S_i$  values in the mixed-phase regime are higher in the C case than in the P case, because of less vapor depletion with fewer hydrometeors (Figure S7). Similarly, efficient condensation in the warm regime and elevated precipitation efficiency lead to the reduction of vapor mixing ratio between 2 and 4 km in the P case (Figures S6e and S6f). Condensation in the warm regime and condensation/deposition/riming in the mixed-phase regime are higher in the P case, resulting in about two times larger latent heating rate and updraft velocity (Figures S6c and S6d). Hence, the increases in liquid/ice contents, latent heating rate, and vertical velocity in the P case result in localized enhancements of precipitation and lightning in the southeast Texas region (Figures 2 and 3).

An additional simulation was performed by implementing the continuous aerosol emission to the C case (referred to as C emis). This sensitivity experiment allows assessment of the impacts of continuous aerosol emissions during the storm, since many major industrial facilities in this region remained operational amid Hurricane Harvey. Comparison between the C emis and C case reveals a profound effect of continuous industrial emissions on precipitation (Figure S8). The spatial distribution of precipitation in C emis (Figures S8a and S8c) is similar to that of the observation (Figure 2a), and the difference in precipitation between the two cases reaches 200–300 mm over a large area downwind of the Houston industrial area (Figure S8c) and about 100 mm in the Houston urban area at 0000 UTC 28 August (Figure S8d). On the other hand, the total accumulated precipitation in C emis is smaller than those of the P case and observation (Figures 2c, 3a, and S8c), indicating that both the initial conditions and continuous emission of aerosol contribute to the flooding during Hurricane Harvey.

Our simulations well reproduce the track (defined by the minimum surface pressure) and intensity (defined by the minimum surface pressure and the maximum wind speed) during the storm evolution, especially considering the first landfall near Corpus Christi and stalling across inland Texas. The simulated track is insensitive to the aerosol perturbations (Figure 3d). A comparison of the minimum pressures and maximum wind speeds between the P and C cases shows a slightly lower surface pressure and higher wind speed, respectively, in the P case during the intensification stage before 26 August (Figures 3e and 3f), indicating an aerosol invigoration effect near the eyewall when CCN efficiently penetrates in. After the landfall, the aerosol effects on the track and intensity are minimal, in contrast with the common notion that elevated aerosols considerably impact the eyewall strength, development, and intensity of hurricanes (Wang et al., 2014). One important reason is that there is an absence of the well-defined eyewall and symmetric rainband for Hurricane Harvey, but the presence of locally intensified precipitation, lightning, and radar reflectivity in the southeast Texas region. Our observations and simulations reveal inhomogeneous distribution and intensity in precipitation, lightning, and radar reflectivity (Figures 1–3).

The extreme precipitation and lightning during Hurricane Harvey are linked to anthropogenic aerosols from industrial emissions, which fundamentally alter the cloud microphysical and thermodynamic processes (Li et al., 2008; Orville et al., 2001; Wang et al., 2011). Elevated aerosols from the industrial sources act as CCN (Figure 4a) to produce more numerous and uniformly distributed but smaller cloud droplets in the warm regime (Figure S9). For warm rain processes (Figure 4b), precipitation formation in the warm regime includes condensation ( $dr/dt \propto (1/r, S_w)$ , where  $r$  is the radius of cloud droplets) and collision/coalescence growth ( $dr/dt \propto r^2$ ) for cloud droplets, which are fast (slow) for small (large) sizes and are slow (fast) for small (large) sizes, respectively. Condensation growth of cloud droplets ( $\sim 10\text{--}20 \mu\text{m}$ ) to reach rain drops ( $\sim 1 \text{ mm}$ ) is too slow at small  $S_w$ , and the formation of warm precipitation requires transition from

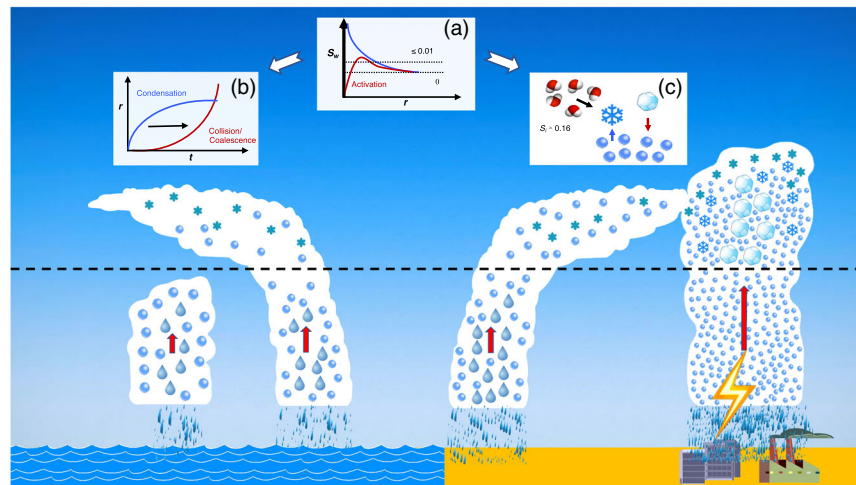


**Figure 4.** Mechanism of industrialization-exacerbated precipitation and lighting, including (a) aerosol activation as CCN, (b) warm rain processes, and (c) mixed-phase processes. The aerosol-hindered warm precipitation is explained by the formation of high concentrations of size-uniform small cloud droplets, which inhibit collision/coalescence. In the absence of warm precipitation, cloud droplets are effectively transported above the freezing level to promote the growth of ice hydrometeors by deposition and riming, leading to enhanced latent heat release and large ice hydrometeors. Also, the coexistence between supercooled droplets and ice hydrometeors (snowflakes and graupel) is essential for cloud electrification. The black dashed line represents the freezing level. The red arrows represent the updraft strength.

condensation to collision/coalescence growth (black arrow in Figure 4b). A higher concentration of cloud droplets results in a larger latent heat release and stronger buoyancy from vapor condensation (Figures S6a–S6d), but a narrow distribution of cloud droplets with smaller sizes effectively inhibits collision/coalescence. In addition to buoyant and cyclonic lifting, suppression of warm rain processes is essential to maintaining the updraft, since falling of raindrops would otherwise induce downdrafts. In the absence of warm precipitation, cloud droplets are effectively transported above the freezing level (black dashed line in Figure 4). In the mixed-phase regime, precipitation formation includes vapor condensation/deposition to supercooled/ice (black arrow in Figure 4c) and accretion of supercooled droplets by ice (riming). Deposition growth of ice is efficient in the mixed-phase regime because of high  $S_i$ , forming large snowflakes that further grow to large graupel by riming. The average  $S_i$  value of 0.16 in the P case at 7 km is higher than that of 0.13 derived from the difference in the saturation vapor pressures between supercooled water and ice, indicating a minor role of deposition growth at the expense of supercooled droplets via the Bergeron process (blue arrow in Figure 4c). The enhanced buoyancy and inhibited rain formation in the warm regime both facilitate vertical lifting and promote the mixed-phase processes, leading to efficient growth of ice hydrometeors by vapor deposition and riming in the P case (Figure 4c). The combination of the increases in the contents of liquid/ice hydrometeors (Figure S5), latent heat release (Figures S6a and S6b), and updraft velocity (Figures S6c and S6d) from the C to P cases significantly modifies the hurricane characteristics (Figure 4).

The remarkable similarity in the geographic distributions between the extreme flooding/lightning during this event and the maximum lightning flash density from the decadal climatology in the south-central United States (Orville et al., 2001) is not a coincidence (Figures S1b and S1c), and both are linked to elevated aerosols from industrial emissions in the Houston region (Levy et al., 2013). Another recent study also showed active warm rain near the eyewall in the early stage on 25 August and significant development of the mixed-phase cloud in rainband on 26 August during Hurricane Harvey (Hu et al., 2020), consistent with our observational and modeling findings.

#### 4. Conclusions

Our combined observational and modeling results unravel the microphysical and thermodynamic evidences to unambiguously establish anthropogenic aerosols as the major factor in regulating the energetics and



flooding during Hurricane Harvey. Forecasts made by the U.S. National Weather Service during this event exhibited major disparity from the observation (Figure S10), largely because of the inability of operational forecast models to account for the aerosol effects (Zhang et al., 2018). In addition, industrial sources likely produce ultrafine particles (Junkermann & Hacker, 2019; Zhang et al., 2012) to contribute to convection and rainfall enhancement, via an analogous invigoration mechanism (Fan et al., 2018). The effects of ultrafine particles on tropical cyclones can only be creditably assessed with measurements of their size distributions and number concentrations and clearly warrant future investigation. The determinant role of industrialization in causing heavy flooding during Hurricane Harvey underscores the importance of representing the aerosol effects in operational forecast and global climate models for hurricane preparedness. It is also imperative that regulatory emission measures are considered to minimize future catastrophic destruction of hurricanes along the highly industrialized coastal area of the Gulf of Mexico.

### Data Availability Statement

Gridded NEXRAD WSR-88D Radar Data can be accessed online (at <http://gridrad.org/index.html>). The Stage IV NCEP/EMC 4 km Gridded precipitation data can be downloaded at EOL website (<https://data.eol.ucar.edu/dataset/21.093>). The National Emission Inventory data can be found at the U.S. EPA website (<https://www.epa.gov/air-emissions-inventories/2011-national-emissions-inventory-nei-data>). The power plants and petrochemical refineries information can be found at the U.S. EIA website ([https://www.eia.gov/maps/layer\\_info-m.php](https://www.eia.gov/maps/layer_info-m.php)). The GOES-R Series Global Lightning Mapper data are available at the NOAA CLAss website (<https://www.bou.class.noaa.gov/saa/products/>). All the WRF model simulation output used for this research can be downloaded from the Caltech website (<http://web.gps.caltech.edu/~yzw/share/Pan-2020-GRL-Harvey>). The code of WRF model used in this study is available online (at <https://www2.mmm.ucar.edu/wrf/users/downloads.html>). All requests for materials in this paper should be addressed to Yuan Wang ([yuan.wang@caltech.edu](mailto:yuan.wang@caltech.edu)).

### Acknowledgments

We were grateful to M. Minamide for providing the satellite data assimilated WRF runs and C. R. Homeyer for accessing the radar reflectivity data. B. P. was supported by a NASA graduate fellowship in Earth Science. Y. W. and J. H. J. acknowledged the support of the Jet Propulsion Laboratory, California Institute of Technology, under contract with NASA. Additional support was provided by the Welch A. Foundation (A-1417) and National Science Foundation AGS-1700727 grants. We also acknowledge the computational support from the Texas A&M High Performance Research Computing (HPRC) facility and appreciate Ping Luo from the Texas A&M HPRC facility for her help on the model setup.

### References

- Bowman, K., & Homeyer, C. R. (2017). GridRad—Three-dimensional gridded NEXRAD WSR-88D radar data. Research Data Archive at the National Center for Atmospheric Research, Computational and Information Systems Laboratory. <https://doi.org/10.5065/D6NK3CR7>. Accessed 28 May 2019.
- Cullen, M. (2013). The Houston lightning mapping array: Network installation and preliminary analysis. In *Master's thesis*. Texas: A & M University. Available electronically from <http://hdl.handle.net/1969.1/151109>
- Emanuel, K. (2005). Increasing destructiveness of tropical cyclones over the past 30 years. *Nature*, 436(7051), 686–688. <https://doi.org/10.1038/nature03906>
- Emanuel, K. (2017). Assessing the present and future probability of Hurricane Harvey's rainfall. *Proceedings of the National Academy of Sciences of the United States of America*, 114(48), 12,681–12,684. <https://doi.org/10.1073/pnas.1716222114>
- Fan, J., Rosenfeld, D., Zhang, Y., Giangrande, S. E., Li, Z., Machado, L. A. T., et al. (2018). Substantial convection and precipitation enhancements by ultrafine aerosol particles. *Science*, 359(6374), 411–418. <https://doi.org/10.1126/science.aan8461>
- Fan, J., Zhang, R., Li, G., Nielsen-Gammon, J., & Li, Z. (2005). Simulations of fine particulate matter (PM<sub>2.5</sub>) in Houston, Texas. *Journal of Geophysical Research*, 110, D16203. <https://doi.org/10.1029/2005JD005805>
- Fan, J. W., Zhang, R. Y., Li, G. H., & Tao, W. K. (2007). Effects of aerosols and relative humidity on cumulus clouds. *Journal of Geophysical Research*, 112, D14204. <https://doi.org/10.1029/2006JD008136>
- GOES-R Algorithm Working Group and GOES-R Series Program (2018). NOAA GOES-R Series Geostationary Lightning Mapper (GLM) Level 2 lightning detection: Events, groups, and flashes. [GLM-L2-LCFA]. NOAA National Centers for Environmental Information. <https://doi.org/10.7289/V5KH0KK6>. Accessed 28 May (2019).
- Goldenberg, S. B., Landsea, C. W., Mestas-Núñez, A. M., & Gray, W. M. (2001). The recent increase in Atlantic hurricane activity: Causes and implications. *Science*, 293(5529), 474–479. <https://doi.org/10.1126/science.1060040>
- Herbener, S. R., van den Heever, S. C., Carrio, G. G., Saleeby, S. M., & Cotton, W. R. (2014). Aerosol indirect effects on idealized tropical cyclone dynamics. *Journal of the Atmospheric Sciences*, 71(6), 2040–2055. <https://doi.org/10.1175/Jas-D-13-0202.1>
- Hu, J., Rosenfeld, D., Ryzhkov, A., & Zhang, P. (2020). Synergetic use of the WSR-88D radars, GOES-R satellites, and lightning networks to study microphysical characteristics of hurricanes. *Journal of Applied Meteorology and Climatology*, 59(6), 1051–1068. <https://doi.org/10.1175/jamc-d-19-0122.1>
- Junkermann, W., & Hacker, J. M. (2019). Ultrafine particles in the lower troposphere: Major sources, invisible plumes, and meteorological transport processes. *Bulletin of the American Meteorological Society*, 99(12), 2587–2602. <https://doi.org/10.1175/bams-d-18-0075.1>
- Khain, A., Cohen, N., Lynn, B., & Pokrovsky, A. (2008). Possible aerosol effects on lightning activity and structure of hurricanes. *Journal of the Atmospheric Sciences*, 65(12), 3652–3677. <https://doi.org/10.1175/2008jas2678.1>
- Knutson, T. R., McBride, J. L., Chan, J., Emanuel, K., Holland, G., Landsea, C., et al. (2010). Tropical cyclones and climate change. *Nature Geoscience*, 3(3), 157–163. <https://doi.org/10.1038/ngeo779>
- Levy, M. E., Zhang, R., Khalizov, A. F., Zheng, J., Collins, D. R., Glen, C. R., et al. (2013). Measurements of submicron aerosols in Houston, Texas during the 2009 SHARP field campaign. *Journal of Geophysical Research: Atmospheres*, 118, 5018–5034. <https://doi.org/10.1002/jgrd.50785>
- Li, G., Wang, Y., Lee, K.-H., Diao, Y., & Zhang, R. (2009). Impacts of aerosols on the development and precipitation of a mesoscale squall line. *Journal of Geophysical Research*, 114, D17205. <https://doi.org/10.1029/2008JD011581>

- Li, G., Wang, Y., & Zhang, R. (2008). Implementation of a two-moment bulk microphysics scheme to the WRF model to investigate aerosol-cloud interaction. *Journal of Geophysical Research*, 113, D15211. <https://doi.org/10.1029/2007JD009361>
- Lynn, B. H., Khain, A. P., Bao, J. W., Michelson, S. A., Yuan, T., Kelman, G., et al. (2016). The sensitivity of hurricane Irene to aerosols and ocean coupling: Simulations with WRF spectral bin microphysics. *Journal of the Atmospheric Sciences*, 73(2), 467–486. <https://doi.org/10.1175/JAS-D-14-0150.1>
- Orville, R. E., Huffines, G., Nielsen-Gammon, J., Zhang, R., Ely, B., Steiger, S., et al. (2001). Enhancement of cloud-to-ground lightning over Houston, Texas. *Geophysical Research Letters*, 28(13), 2597–2600. <https://doi.org/10.1029/2001GL012990>
- Pan, B., Wang, Y., Hu, J., Lin, Y., Hsieh, J.-S., Logan, T., et al. (2018). Impacts of Saharan dust on Atlantic regional climate and implications for tropical cyclones. *Journal of Climate*, 31(18), 7621–7644. <https://doi.org/10.1175/jcli-d-16-0776.1>
- Patricola, C. M., & Wehner, M. F. (2018). Anthropogenic influences on major tropical cyclone events. *Nature*, 563(7731), 339–346. <https://doi.org/10.1038/s41586-018-0673-2>
- Reynolds, R. W., Smith, T. M., Liu, C., Chelton, D. B., Casey, K. S., & Schlax, M. G. (2007). Daily high-resolution-blended analyses for sea surface temperature. *Journal of Climate*, 20(22), 5473–5496. <https://doi.org/10.1175/2007JCLI1824.1>
- Rosenfeld, D., Woodley, W. L., Khain, A., Cotton, W. R., Carrio, G., Ginis, I., & Golden, J. H. (2012). Aerosol effects on microstructure and intensity of tropical cyclones. *Bulletin of the American Meteorological Society*, 93(7), 987–1001. <https://doi.org/10.1175/Bams-D-11-00147.1>
- Souri, A. H., Choi, Y., Kodros, J. K., Jung, J., Shpund, J., Pierce, J. R., et al. (2020). Response of hurricane Harvey's rainfall to anthropogenic aerosols: A sensitivity study based on spectral bin microphysics with simulated aerosols. *Atmospheric Research*, 242, 104965. <https://doi.org/10.1016/j.atmosres.2020.104965>
- Trenberth, K. (2005). Uncertainty in hurricanes and global warming. *Science*, 308(5729), 1753–1754. <https://doi.org/10.1126/science.1112551>
- U.S. Environmental Protection Agency (2011). *National Emissions Inventory, version 2 (Technical Support Document)*.
- van Oldenborgh, G. J., van der Wiel, K., Sebastian, A., Singh, R., Arrighi, J., Otto, F., et al. (2017). Attribution of extreme rainfall from Hurricane Harvey, August 2017. *Environmental Research Letters*, 12(12), 124009. <https://doi.org/10.1088/1748-9326/aa9ef2>
- Wang, Y., Lee, K.-H., Lin, Y., Levy, M., & Zhang, R. (2014). Distinct effects of anthropogenic aerosols on tropical cyclones. *Nature Climate Change*, 4(5), 368–373. <https://doi.org/10.1038/nclimate2144>
- Wang, Y., Wan, Q., Meng, W., Liao, F., Tan, H., & Zhang, R. (2011). Long-term impacts of aerosols on precipitation and lightning over the Pearl River Delta megacity area in China. *Atmospheric Chemistry and Physics*, 11(23), 12,421–12,436. <https://doi.org/10.5194/acp-11-12421-2011>
- Zhang, R., Khalizov, A. F., Wang, L., Hu, M., & Xu, W. (2012). Nucleation and growth of nanoparticles in the atmosphere. *Chemical Reviews*, 112(3), 1957–2011. <https://doi.org/10.1021/cr2001756>
- Zhang, R., Wang, G., Guo, S., Zamora, M. L., Ying, Q., Lin, Y., et al. (2015). Formation of urban fine particulate matter. *Chemical Reviews*, 115(10), 3803–3855. <https://doi.org/10.1021/acs.chemrev.5b00067>
- Zhang, W., Villarini, G., Vecchi, G. A., & Smith, J. A. (2018). Urbanization exacerbated the rainfall and flooding caused by hurricane Harvey in Houston. *Nature*, 563(7731), 384–388. <https://doi.org/10.1038/s41586-018-0676-z>
- Zhao, C., Lin, Y., Wu, F., Wang, Y., Li, Z., Rosenfeld, D., & Wang, Y. (2018). Enlarging rainfall area of tropical cyclones by atmospheric aerosols. *Geophysical Research Letters*, 45, 8604–8611. <https://doi.org/10.1029/2018GL079427>